The Magnetic-Resonance Force Microscope: A New Tool for High-Resolution, 3-D, Subsurface Scanned Probe Imaging

P. CHRIS HAMMEL, DENIS V. PELEKHOV, PHILIP E. WIGEN, MEMBER, IEEE, TIMOTHY R. GOSNELL, MELISSA M. MIDZOR, AND MICHAEL L. ROUKES

Invited Paper

The magnetic-resonance force microscope (MRFM) is a novel scanned probe instrument which combines the three-dimensional (3-D) imaging capabilities of magnetic-resonance imaging with the high sensitivity and resolution of atomic-force microscopy. It will enable nondestructive, chemical-specific, high-resolution microscopic studies and imaging of subsurface properties of a broad range of materials. The MRFM has demonstrated its utility for study of microscopic ferromagnets, and it will enable microscopic understanding of the nonequilibrium spin polarization resulting from spin injection. Microscopic MRFM studies will provide unprecedented insight into the physics of magnetic and spin-based materials. We will describe the principles and the state-of-the-art in magnetic-resonance force microscopy, discuss existing cryogenic MRFM instruments incorporating high-Q, single-crystal microresonators with integral submicrometer probe magnets, and indicate future directions for enhancing MRFM instrument capabilities.

Keywords—Force detection, magnetic resonance, magnetic-resonance force microscope (MRFM), scanning probe, spin, spintronics.

I. INTRODUCTION

Recent years have seen rapid advancement of the field of spin electronics (or spintronics), a new research arena that combines the fields of electronics and magnetism with the goal of generating a new electronics technology made more powerful by exploiting electronic spin [1]. Undoubtedly, successful fabrication of practical spintronic devices is a very challenging task that will advances in the areas of materials, characterization, and measurement.

Crucial for spintronics is the recently demonstrated ability to electrically inject spin-polarized currents into semiconductors [2], [3]. This represents a very significant step toward incorporating devices based on electronic spin into conventional semiconductor electronic devices. However, an improved understanding of the dependence of electrical spin injection properties on device fabrication, materials used, and the nature of the interfaces will be essential in order to optimize spintronic device performance and enable their incorporation into conventional semiconductor electronics.

In order to meet these challenges it will be essential to have tools capable of imaging and evaluating the characteristics of various components buried within these devices and, very importantly, of the interfaces between various components. This paper describes a unique tool capable of providing this information: the magnetic-resonance force microscope (MRFM). We will present the general principles of MRFM operation, discuss the avenues that will be pursued in application of the MRFM in studies of spintronics devices, present the current state of MRFM development, and discuss future directions.

II. MAGNETIC-RESONANCE FORCE MICROSCOPY FOR SPINTRONICS

High-resolution imaging technologies such as atomic-force microscopy (AFM) and magnetic-resonance imaging (MRI) have had substantial impact in fields ranging from electronic and structural materials to medical science. AFM provides atomic scale resolution but is essentially limited to surface studies, as is the case for all other conventional scanned probe microscopies. MRI is a fully

three-dimensional (3-D) , noninvasive imaging technology which employs an applied magnetic field gradient $\nabla \mathbf{B}$ to distinguish magnetic-resonance signals arising from different spatial locations. Although it is possible to generate very large field gradients, the spatial resolution of MRI is currently limited to dimensions greater than tens or even hundreds of micrometers due to the poor sensitivity of the inductive technique of magnetic-resonance detection. Clearly, the ideal prospect would be to attain the high resolution of AFM, while retaining the 3-D imaging characteristics of MRI. This is the essence of the MRFM.

The MRFM offers the possibility of shrinking the linear dimension of resolved volumes into the submicrometer regime, with the clear possibility of achieving atomic-scale resolution. It is likely that the MRFM will ultimately match the resolution achievable in scanning probe microscopes such as scanning tunneling and atomic force microscopes. The MRFM has several important strengths among scanned probe microscopes.

- The imaging field is 3-D; its extent below the scanned surface is determined by the spatial dependence of the field gradient.
- Because each magnetic nucleus has a unique gyromagnetic ratio, nuclear magnetic resonance imaging is chemical-species specific.
- The well-developed and validated theory of magnetic-resonance interactions provides a reliable basis for the design and operation of imaging instruments.

The MRFM is a novel scanning probe method based on mechanical detection of magnetic resonance that is currently being developed by several experimental groups in the world. It will provide a unique and powerful approach to measuring the spatial and temporal decay of injected, nonequilibrium spin polarization in electrically injected systems. Several questions that remain to be answered will be crucial in the optimization of processes and the application of spin injection devices. Among these are the temporal and spatial decay rates of the injected nonequilibrium spin polarization, and a detailed characterization of the behavior of the spin-polarized currents in the immediate vicinity of the interface. Spatially resolved mapping of the nonequilibrium spin polarization resulting from a steady-state injection current will allow direct measurement of the decay of the spin polarization as a function of distance from the injection interface, and thus, direct measurement of the spatial decay rate. Imaging in the plane of the interface could provide crucial insight into the lateral homogeneity. If inhomogeneities exist, these studies would provide a detailed, quantitative basis for modification of fabrication processes to improve injection properties.

In the following sections we will discuss the experimental challenges faced in applying the MRFM to studies of spin electronic systems. Section III discusses the principles of MRFM measurements, Section IV discusses the details of the interaction between the micromagnetic probe tip and the sample that enables sensitive detection of magnetic resonance. Clearly, a crucial issue is the spatial resolution achievable by this technique; this analysis enables a quanti-

tative understanding of the sensitivity of our instrument and hence estimates of spatial resolution; these are discussed in Section V. In Section VI, we discuss the role MRFM can play in studying and imaging the microscopic ferromagnets that serve to generate spin-polarized currents. Finally, Section VII addresses generating images from MRFM data.

III. MRFM Principles

First proposed in the early 1990s [4], [5], the MRFM is proving to be a quite versatile instrument that has been demonstrated in a variety of magnetic-resonance experiments: electron spin resonance [6], [7], nuclear magnetic resonance [8], and ferromagnetic resonance [9], [10].

The method relies on the coupling between a sample magnetic moment $\boldsymbol{m}$ and a probe magnet mounted on a compliant micromechanical resonator via the force of magnetic interaction

$$\boldsymbol{F}(\boldsymbol{x}, t) = -\left[\boldsymbol{m}(\boldsymbol{x}, t) \cdot \nabla\right] \boldsymbol{B}_{\text{probe}}(\boldsymbol{x}). \tag{1}$$

The strength of this interaction is proportional to the gradient of the inhomogeneous magnetic field of the probe magnet. This force of interaction is measured through detection of the displacement of the resonator that is deflected by the applied force.

The force sensitivity of the method is ultimately limited by the thermomechanical force noise F_n of the detector. This noise depends on temperature T (k_B is Boltzmann's constant) and detection bandwidth $\Delta \nu$, as well as mechanical characteristics of the resonator, e.g., its spring constant k, characteristic frequency f_c, and quality factor Q [7], [11], [12]

$$F_n = \sqrt{\frac{2kk_B T \Delta \nu}{\pi Q f_c}}. \tag{2}$$

In order to generate a force at f_c, the magnetic moments under study are made to vary at this frequency. This is achieved by modulating either the microwave excitation field H_1 or the applied field H_0. In the case where recovery of the spin magnetization is rapid compared to $1/f_c$, the microwave excitation is used to suppress (saturate) the electron-spin magnetization. Amplitude modulation (AM) of H_1 will periodically suppress the magnetization in the resonant volume. Frequency modulation (FM) of H_1 (equivalent to applied field modulation through (3)) displaces the resonant volume (or "sensitive slice") in the sample by a distance $z_{\text{mod}} \simeq \Delta f_{\text{mod}}/\gamma|\nabla_{\mathbf{z}}\mathbf{B}|$. FM is an attractive approach because it minimizes spurious forces on the sensitive mechanical detector arising from coupling to time-varying applied fields. However, because it causes the position of the sensitive slice to oscillate, the spatial resolution in this case is given by the convolution of Δz_{res} and z_{mod}.

The time variation of the sample spin magnetization results in a harmonic excitation force acting on the probe resonator. If this excitation is performed at the natural frequency f_c of the resonator, its displacement is magnified by its quality factor Q, which can be as high as 10^5, compared

to the displacement resulting from a dc force of the same magnitude. The combination of high magnetic field gradients from microscopic magnetic probes and high-quality factors makes detection of a single-electron spin resonance theoretically possible. Because spatial resolution is limited by the ability to detect the signal from a volume element to be imaged, this high sensitivity holds the key to obtaining extremely high spatial resolution.

The second key function of the magnetic field gradient, in addition to coupling the sample spin magnetization to the sensitive force detector, is, as in MRI, the definition of the volume of material hundreds of angstroms or even micrometers beneath the surface that will be studied.

The electron spin precesses at its Larmor frequency f_L which is proportional to the magnetic field B it experiences

$$f_L = g\mu_B B. \qquad (3)$$

Here g is the g-factor for the given species in the host material and μ_B is the Bohr magneton. If the applied field varies spatially, then the correspondence between applied field and resonant frequency translates into a correspondence between position and frequency: spins too close to the magnetic tip experience a field too large to be in resonance with the applied microwave field $H_1 = H_1^0 \cos(2\pi f_{\mathrm{mw}} t)$ and so are unaffected, and similarly spins too far from the tip are not influenced by H_1. Only those spins for which $f_L = f_{\mathrm{mw}}$ to within the electron spin magnetic-resonance linewidth Δf_{lw} will respond to H_1. The strength of the field gradient $|\mathbf{\nabla_z B}|$ and Δf_{lw} determines the dimensions (say z_{sl}) of the selected resonant volume

$$z_{\mathrm{sl}} \simeq \frac{\Delta f_{\mathrm{linewidth}}}{\gamma |\mathbf{\nabla_z B}|}. \qquad (4)$$

Field gradients sufficiently large to obtain angstrom scale resolution can be obtained using lithographically defined permanent magnets; the key to obtaining high spatial resolution is to optimize the sensitivity of the microscope. While current conventional magnetic-resonance detection limits are $\sim 10^{15}$ nuclear spins, the theoretical limit for mechanical detection is a *single nuclear spin*. This enhanced sensitivity allows one to reduce the volume of the sample isolated for study (i.e., allows one to improve the spatial resolution of the microscopic study) while maintaining adequate signal-to-noise ratios.

The general concept of the method allows two major MRFM architectures. One places the sample on the mechanical resonator which is then coupled to an external probe magnet. This approach allows use of a relatively large probe magnet with well-known magnetic properties. However, the requirement that samples be placed on the resonator severely limits the applicability and usefulness of a microscope based on this design. The approach we are currently pursuing in our research involves a micromagnetic probe mounted directly on the mechanical resonator brought in the close vicinity of the sample. This will allow true scanning operation on a sample of arbitrary size, however, the fabrication of a micromagnet with well-known magnetic properties
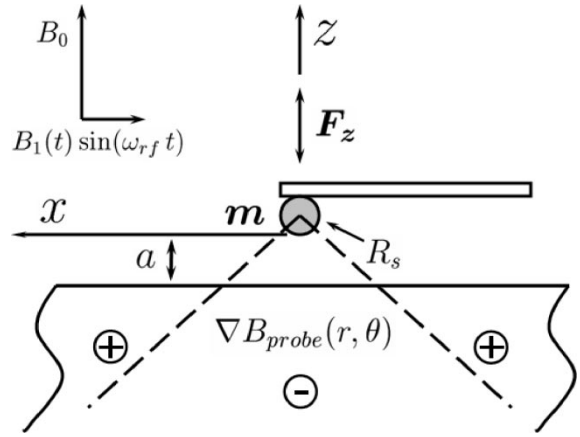

Fig. 1. Schematic diagram of the geometry of an MRFM. The spherical micromagnet (radius R_s) on the mechanical resonator produces an extremely inhomogeneous magnetic field that serves two purposes: i) it couples the mechanical resonator to the magnetic moments in the sample, and ii) it defines the spatial regions of the sample where the magnetic-resonance condition is met. Magnetic-resonance techniques can be employed to manipulate magnetic moments in the sample thus generating time variable force on the mechanical resonator at its resonance frequency that will drive it into oscillation.

is challenging. For this reason, accurate mapping of the magnetic field of a probe micromagnet is very important for the development of the MRFM.

Reliable interpretation of MRFM signals requires thorough and detailed understanding of the interaction between the micromagnetic probe and the sample. Here we address this problem is some detail.

IV. THEORY OF MRFM PROBE–SAMPLE INTERACTION

We introduce a model representing a typical scanning MRFM geometry (Fig. 1) which will enable both analytical and numerical analysis of the probe–sample interaction, depending on experimental parameters. The probe magnet is modeled as a sphere of a radius R_S uniformly magnetized along the direction of the external magnetic field $\boldsymbol{B}_0$. This magnet is mounted on a mechanical resonator with resonant frequency $f_c = \omega_c/2\pi$. The sample is assumed to be uniformly magnetized with its magnetization given as $\boldsymbol{m} = \{0, 0, m_z\}$. The in-plane components of the magnetization are ignored because their precession frequency $\omega_L \gg \omega_c$. Taking into account that the resonator can oscillate only along $\hat{z}$ direction, the probe–sample interaction is given by

$$F_z = -\boldsymbol{e}_z \cdot \int d^3 r \, [\boldsymbol{m}(\boldsymbol{r}) \cdot \boldsymbol{\nabla}] B_{\mathrm{tot}}(\boldsymbol{r}) \qquad (5)$$

where

$$\boldsymbol{B}_{\mathrm{tot}}(\boldsymbol{r}) = \boldsymbol{B}_{\mathrm{probe}}(\boldsymbol{r}) + \boldsymbol{B}_0.$$

Since $|\boldsymbol{B}_0| \gg |\boldsymbol{B}_{\mathrm{probe}}(\boldsymbol{r})|$, we can assume $\boldsymbol{B}_{\mathrm{tot}}(\boldsymbol{r}) \| \boldsymbol{e}_z$.

We can manipulate the sample magnetization by means of various rf-modulation techniques in order to generate an alternating force on the mechanical magnetic-resonance detector. For the purposes of our analysis, AM of the rf power at the resonant frequency of the mechanical resonator (the simplest modulation method to analyze) is used. We assume

that the spins in the sample are always in dynamical equilibrium; this assumption is valid if the spin-lattice relaxation time T_1 of the sample material is much shorter than the oscillation period of the mechanical resonator.

AM generates a time-dependent force with a strong Fourier component at the resonance frequency of the mechanical resonator with an amplitude given by

$$F_z^{f_c} = -\boldsymbol{e}_z \cdot \int d^3 r \left[\boldsymbol{\delta m}(\boldsymbol{r}) \cdot \boldsymbol{\nabla}\right] \boldsymbol{B}_{\text{tot}}(\boldsymbol{r}) \qquad (6)$$

where $\boldsymbol{\delta m}(\boldsymbol{r})$ is the local change of sample magnetization during a single cycle of rf-modulation.

It turns out that analytical integration of (6) is relatively straightforward only for a few symmetric limiting cases and is extremely complicated for a general experimental MRFM geometry. However, these cases prove to be valuable guides for understanding this interaction [13]. Due to the limiting nature of the available analytical solutions, quantitative comparisons with experiment can be achieved only by numerical integration of (6). Numerical solution allows us to analyze arbitrary probe sample geometries and more realistic models of the probe micromagnet. The detailed description of both analytical and numerical approaches is given in [13].

The numerically calculated analysis of the probe sample interaction displayed in Fig. 2 shows the evolution of both the sensitive slice and the force slice under typical experimental conditions. The external magnetic field B_0 is changed continuously while the frequency of the rf field ω_{rf} is kept constant. The concept of the "sensitive slice" refers to the sample volume in which magnetic moments are on resonance with the rf field, that is, the region where the condition $\omega_{\text{rf}} = \gamma B_{\text{tot}}(\boldsymbol{x})$ is satisfied. The right-hand panel of Fig. 2 shows the spatial variation of the suppression of the sample spin magnetization by the rf field. The concept of the "force slice" describes coupling of the magnetic moments in the sample to the probe magnet on the mechanical resonator. This is the volume of the sample that actually contributes to the alternating force driving the mechanical resonator, that is, it is the volume where the integrand of (6) is nonzero. The left-hand panel of Fig. 2 shows the local force contribution as a function of spatial position within the sample. It is important to mention that the sign of the local force contribution is defined by the sign of the appropriate component of the gradient of magnetic field of the probe. Due to the dipolar nature of the probe magnetic field, this sign depends on the position of the point of interest relative to the probe magnet. The line on the left-hand panel of Fig. 2 shows where this component of the gradient passes through zero and changes sign. This figure makes clear that the force contributions from different parts of the sample can have opposite signs [Fig. 2(a)], and can cancel one another under certain conditions.

The model developed in [13] allows us to predict the evolution of the MRFM signal as experimental parameters are changed. Figure 3 shows the MRFM signal calculated for various probe–sample separations. It can be seen that each curve exhibits a strong peak near the resonant field. The position of this peak is independent of the magnitude of the probe–sample separation. However, as the probe is brought
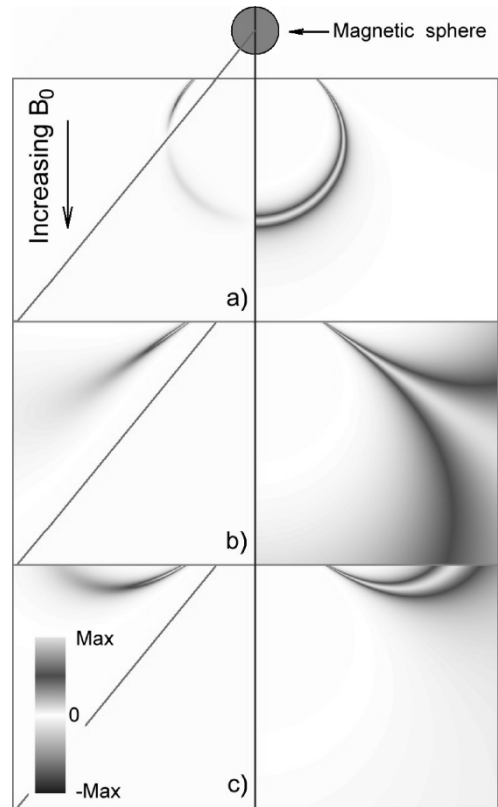

Fig. 2. Calculation of the sensitive slice shape (right-hand panels) and the force slice (left-hand panels) for different values of the external field B_0. For all panels $\omega_{\text{rf}}/\gamma = 10\,000$ G and $a/R = 1$. The force slice is weighted by the volume element. The purple line on the left (force slices) marks the angle at which the local force changes sign (see also Fig. 1). (a) ($B_0 = 9985$ G) show typical sensitive slices as shells of constant field for $\gamma B_0 < \omega_{\text{rf}}$. (b) show the situation for $\gamma B_0 = \omega_{\text{rf}}$. In this case, the gradient is very small in the regions where the resonance condition is met, so the ratio of the linewidth to the gradient is very large, hence, a large volume of sample meets the resonance condition. The conventional concept of a typical length scale set by the width z_{sl} of the sensitive slice ($z_{\text{sl}} \approx \delta B_{\text{linewidth}}/\nabla B$) breaks down in this case. (c) $\gamma B_0 > \omega_{\text{rf}}$ ($B_0 = 10\,005$ Gauss). Here the shape of the sensitive slice is approximately toroidal.

closer to the surface of the sample, the leading edge of the signal shifts to lower values of external magnetic field. The offset of the leading edge of the signal relative to the main peak is a direct measure of the magnitude of the probe magnetic field at the surface of the sample directly below the probe; this increases as the probe–sample separation is decreased.

The main peak of the signal corresponds to the case when the majority of the sample is in resonance and the concept of a well-defined sensitive slice has broken down, Fig. 2(b). The region of interest for the MRFM operating as a high spatial resolution subsurface imaging tool is near the leading edge of the signal where the force slice is well defined and the number of spins contributing to the signal, and thus the signal itself, is small.

V. EXPERIMENTAL RESULTS FOR MRFM SENSITIVITY

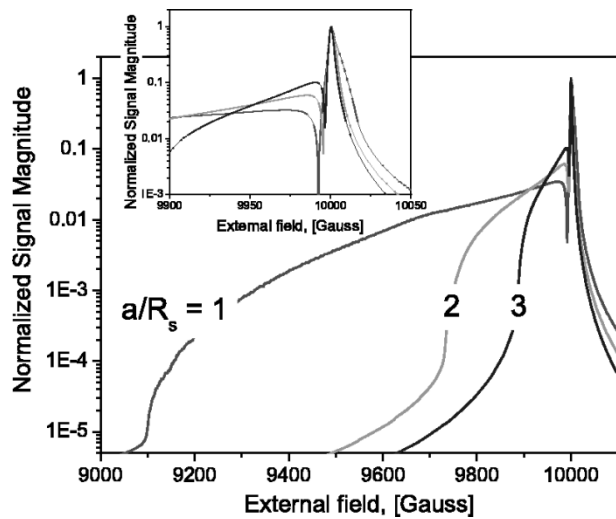We have experimentally observed the evolution of the leading edge of MRFM signal. The MRFM was used to

Fig. 3. Numerical calculation of the MRFM signal versus external magnetic field for various sample–probe separations a measured in units of the radius of the probe magnet R_S. This calculation was performed for a semi-infinite bulk sample assuming that the resonant field in the absence of the probe magnet is 10 000 G. The inset shows an expanded view of the main resonance peak.

Fig. 4. The electron spin resonance signal from a 100-nm DPPH film at various probe–sample separations detected using FM of the rf field at $T = 4$ K. Arrows mark the position of the peak corresponding to the leading edge of the signal. The inset shows the leading edge signal detected at 2.1-μm probe–sample separation. The microscope sensitivity is limited by nonthermal low-frequency noise of uncertain origin.

Fig. 5. Magnetic field of the probe magnet vs. the distance from its tip. The solid curve presents the result of the micromagnetic simulations of the expected magnetic field of the probe magnet used in the experiment. The solid squares are experimentally measured values of the field of the probe magnet.

detect the electron spin resonance (ESR) signal from a 100-nm-thick DPPH film at $T = 4$ K. We chose to apply FM of the applied microwave radiation to manipulate the electron spins in the sample because AM creates an undesirable excitation of the mechanical resonator complicating detection of weak signals. In the case of FM, the power of the rf radiation is kept constant as its frequency is modulated at f_c. Though the FM approach reduces the coupling of the rf field to the mechanical resonator, it generates an MRFM signal that is the derivative with respect to the applied field of the signal produced by AM excitation that was discussed in the previous section. In the FM case, the leading edge of the signal appears as a peak that shifts its position as the probe is moved toward the sample.

Fig. 4 shows a series of MRFM signals recorded at various probe–sample separations. As expected from the analysis presented in the previous section, we observe a large signal at the resonant field (the field at which spins would be resonant in the absence of the probe magnetic field) which is independent of the probe position, and a much smaller leading edge feature that corresponds to the sensitive slice entering the sample. The latter feature shifts to lower values of the external magnetic field as the probe approaches the sample surface. The field at which this feature appears provides a direct measure of the magnetic field of the probe magnet at the sample surface allowing us to experimentally measure the probe field. The filled squares in Fig. 5 show the increase of the field of the probe magnet with decreasing separation. The solid curve presents the results of micromagnetic simulations of magnetic field of a micromagnet using parameters that describe the probe magnet used in the experiment. The experimental data is in excellent agreement with the theoretical curve.

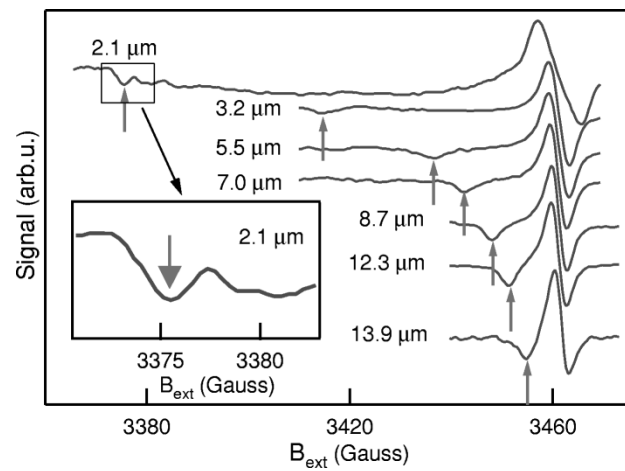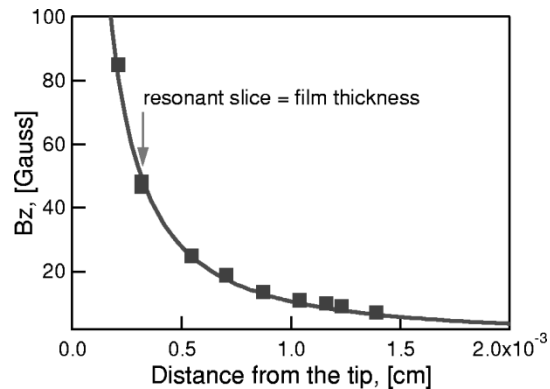Precise understanding of the field of a particular probe magnet enables us, using the model of probe–sample interaction previously described, to predict the shape of the sensitive slice for a scanning probe–sample geometry. This ability is crucial to the development of subsurface 3-D MRFM imaging such as is used in conventional MRI. In practice, this method will be based on a data processing technique which extracts the 3-D image from a collection of intersecting subsurface sensitive slices obtained at various spatial probe positions and values of external magnetic field as discussed later in Section VII. The field profile of the probe magnet determines the so-called "point response function" of the microscope; thorough knowledge of this function is crucial for deconvolving images from MRFM data.

Knowledge of the field of the probe magnet has also enabled us to estimate the number of spins contributing to the measured signal at various values of external magnetic field and probe–sample separation. The leading edge feature observed at a probe–sample separation of 2.1 μm corresponds

to a signal from approximately 10^4 fully polarized electron spins. The signal strength observed in the inset to Fig. 4 is consistent with our estimate of the single-shot detection sensitivity of our microscope (based on knowledge of the cantilever parameters k, f_c, and Q and the strength of the field gradient) of 10^3 fully polarized electron spins. Improvements in noise-rejection techniques are expected to improve the sensitivity of our microscope by an order of magnitude in the near future.

The spatial resolution of the microscope is determined by its sensitivity; in particular, a resolvable volume of a sample must provide a signal force equal to the thermomechanical detector force noise. The spatial resolution obtained in a spintronic device given 1000 spin sensitivity is then determined by the polarization of the spin current and the carrier density. For instance, for a carrier concentration of 10^{17} cm^{-3} and a spin polarization of 50% the single-shot detectable volume would be $\sim (0.3\ \mu\text{m})^3$. In imaging the polarized spin density resulting from spin polarized current injection it will be essential to consider the influence of the inhomogeneous magnetic fields arising from the ferromagnetic injector and the micromagnetic MRFM probe since such fields could modify the magnetization.

One might be concerned that the magnetic-resonance signal arising from the ferromagnetic injector, which could be quite strong since the electronic moments are fully polarized, will mask the signal associated with the injected spin polarized current in the paramagnetic semiconductor. In the following section, we discuss MRFM signals arising from a ferromagnet. We will see that such ferromagnetic-resonance (FMR) signals occur at an applied magnetic field determined by the strong interactions among spins, and, as a consequence, this field will, in general, be substantially different from the resonance field of noninteracting electronic moments in the paramagnetic semiconductor. In particular, for the external field applied perpendicular to the plane of the ferromagnetic film the field that will lead to resonance in the paramagnet will be insufficient for resonance in the ferromagnet, so the injector will produce no MRFM signal. Thus, by exploiting its 3-D imaging capabilities, the MRFM will be able to "see" through the injector to the buried paramagnet.

VI. Application of MRFM to Imaging of Microscopic Ferromagnets

We have recently demonstrated [14] the application of the MRFM to FMR imaging of micromagnetic systems. Spatially resolved FMR imaging presents a challenge for microscopic magnetic imaging because of the strong interaction between the electronic moments; this renders the resonance frequency a nonlocal function of the applied magnetic field. As a consequence, the ferromagnetic dynamics are typically determined by sample dimensions and the concept of the "sensitive slice" presented earlier in the paper is not generally valid. However, our recent work [14] has shown that in the presence of a sufficiently strong probe magnetic field, the intensities of the ferromagnetic modes of the sample are strongly enhanced, indicating a local modification of the wavevector of magnetostatic modes selected by the probe tip. These results suggest that further increase of the probe field will enable the FMR modes to be determined by the probe field independent of sample geometry.

This effect has been demonstrated in ferromagnetic resonance force microscopy (FMRFM) experiment performed on micrometer-scale samples of yttrium iron garnets (YIG) [15]. The rectangular samples with thickness $d \simeq 3\ \mu$m, widths $w = 10$ and $20\ \mu$m, and lengths ranging from $L = 10$ to 320 μm were fabricated out of single-crystal YIG films by means of optical lithography and ion-beam milling.

There are three main regimes of FMRFM operation defined by the strength of magnetic field introduced in the sample by the probe magnet. In the first regime, the probe magnet produces a negligible (a few Gauss) additional magnetic field ΔB at the sample. In practice, this corresponds to a probe–sample separation of approximately 10 μm. The magnitude of this field is peaked directly under the magnetic probe tip and decreases as a function of in-plane distance from the probe tip. Under these conditions of weak probe field, the dispersion relation (the relationship between the externally applied magnetic field and the resonant frequency of a magnetostatic mode) is defined by the dimensions of the whole sample and its magnetic properties. In this unperturbed case, the relation between the spatial variation of the precessing magnetic moment and its frequency ω is well described by existing theory [16]–[18].

Such an FMRFM spectrum is shown in Fig. 6(a). The resonant frequencies and intensities of the modes are entirely determined by the sample dimensions and the uniform externally applied magnetic field. The experimental data is in a very good agreement with the theoretical values (Fig. 6(b)).

However, unlike in the case of a conventional FMR detection, even in the regime of weak probe magnetic field its influence cannot be entirely disregarded. Even the small perturbation introduced by the probe placed slightly off sample center breaks the symmetry of magnetostatic modes in the sample and results in observation of a "hidden" even ($n = 2$) mode [Fig. 6(a)] which is not observed in conventional FMR detection due to zero net transverse magnetic moment of such a mode.

This local perturbation opens a new avenue for *local* FMR imaging in micromagnetic systems using FMRFM. As the probe magnet approaches the surface of the sample, its magnetic field introduces an ever stronger perturbation to the dispersion relation. These experiments revealed that in this intermediate regime of probe magnetic field—$\Delta B \approx 20$–50 G—the intensity of modes whose half-wavelength matches the effective range of the tip field l are significantly increased. However, the resonance field of such a mode at a given frequency is still largely determined by the dimensions of the sample. As shown in Fig. 7, as the probe magnet approaches the sample surface, the relative intensity of the fundamental mode decreases while that of these particular higher order modes strongly increases.

This result can be qualitatively explained within a simple model of the ferromagnetic dynamics in the presence of a
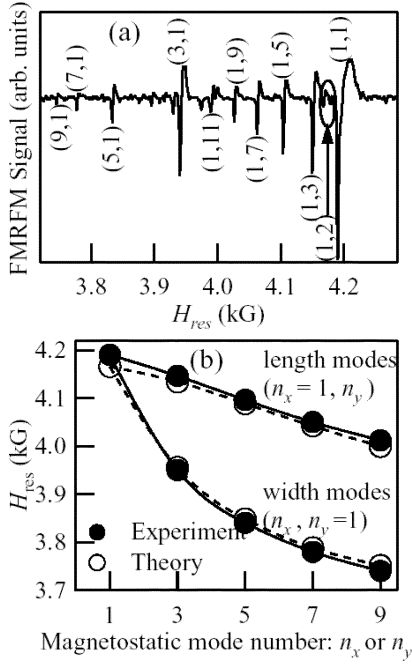
Fig. 6. (a) An FMR spectrum from a $20 \times 80 \ \mu$m YIG sample obtained using the MRFM showing the mode numbering (n_x, n_y). The arrow indicates the "hidden" $n_y = 2$ mode. We observe this mode when the tip is displaced laterally from sample center by 5–25 μm along the long axis of the sample. (b) The dependence of resonance field $H_{\rm res}$ on mode number for this sample.
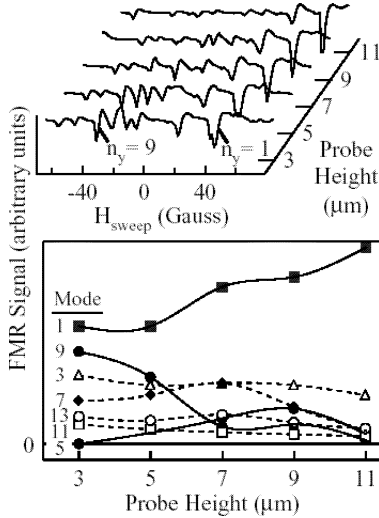

Fig. 7. (Top) Spectra of the $20 \times 160 \ \mu$m sample reveal dramatic enhancement of the modes in the vicinity of $n = 9$ as the probe magnet is brought to within 3 μm of the sample surface. (Bottom) The dependencies of mode intensities on this tip–sample separation are shown.

nonuniform magnetic field profile produced by the probe magnet. The integral equation describing the behavior of the sample magnetization under the influence of the nonuniform magnetic field can be solved numerically revealing periodic maxima in the FMR intensity for modes whose half-wavelengths match the spatial extent of the magnetic field of the probe, in good qualitative agreement with the experimental data.

These experimental results combined with the theoretical model indicate the possibility of doing true local FMR spectroscopy in magnetic systems by using MRFM in the regime of a strong probe magnetic field ΔB. These fields will allow excitation of the magnetostatic modes that will be stable only in the region of the strong perturbation field. The resonant frequencies and intensities of these modes will be defined by the local magnetic properties of the sample. The spatial resolution of FMRFM in this regime of operation will be ultimately limited by the size of the probe magnet and could conceivably be as low as $\sim$100 nm.

VII. DECONVOLUTION OF MRFM IMAGE DATA

As discussed in Section IV, MRFM image data is obtained by scanning the cantilever over a specified spatial range. The spatial extent of the region in which the probe tip interacts with the magnetic polarization of the sample (a thin shell where the magnetic-resonance condition is met) is much larger than the length scale that characterizes the spatial resolution (the thickness of this shell). This extended but well-defined region of interaction makes it possible to probe buried interior volumes by scanning. The price paid is that processing of the as-captured MRFM image data is required in order to deconvolve the delocalized response of the cantilever and reveal the spatial distribution of the magnetization.

These issues can be illustrated by considering Fig. 8. First, Fig. 8(a) shows a 3-D rendering of the sensitive slice for typical MRFM operating parameters in use today. In particular, the probe is positioned $\sim$1000 nm above the depicted region; the range of the plot is 600 nm $\times$ 600 nm in the horizontal directions and 150 nm in the vertical direction. For this case, we assume a probe consisting of a spherical micromagnet. Fig. 8(b) shows an analogous rendering of a fictitious sample with a relative polarized-spin density indicated by the color bar at the bottom of the figure. When the magnetization density of Fig. 8(b) is scanned by the MRFM probe, the cantilever response will be

$$\Re(\boldsymbol{r}) = \int \Phi(\boldsymbol{r} - \boldsymbol{r}')m(\boldsymbol{r}')d^3r' \tag{7}$$

where $m(\boldsymbol{r}')$ is the magnetization density of the sample and $\Phi(\boldsymbol{r})$ is the point-response function of the MRFM transducer. This function is identical in form to the sensitive slice of Fig. 8(a) except for an inversion of coordinates $\boldsymbol{r} \to -\boldsymbol{r}$; the point is that the position coordinate $\boldsymbol{r}$ in (7) denotes the position of the probe rather than a position within the sample. With the addition of Gaussian noise, Fig. 8(c) shows x, y, and z slices through the data set that results from (7) when the magnetization is sampled by the MRFM on a $32 \times 32 \times 32$ grid. The noise level is chosen so that the signal-to-noise ratio at the position of maximum response is only 5.

The image deconvolution or *reconstruction* problem can now be succinctly stated: With the input data of Fig. 8(c) and knowledge of the functional form of the sensitive slice, Fig. 8(a), what computational procedure best recovers the actual magnetization density shown in Fig. 8(b)?
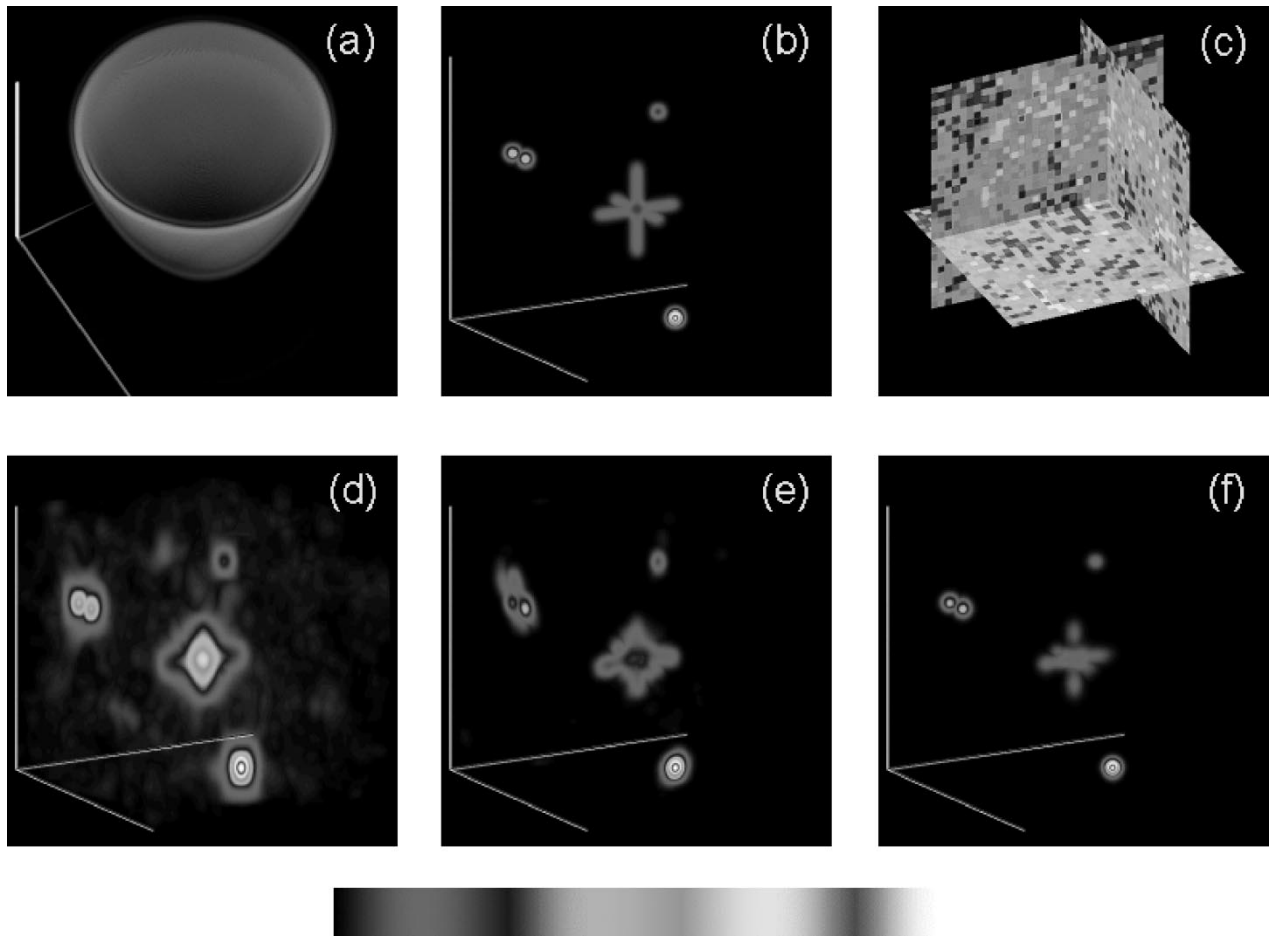
Fig. 8. Comparison of MRFM image deconvolution for three different techniques. (a) 3-D rendering of the MRFM sensitive slice. (b) Synthetic truth image. (c) Slices through the resulting data in x, y, and z directions when (b) is convolved with (a) and plotted as a function of position of the MRFM probe. The noise is chosen so that the signal-to-noise ratio at the position of maximum response is 5. The sampling is on a $32 \times 32 \times 32$ grid. (d) Deconvolution by Wiener optimal filtering. (e) Deconvolution by maximum likelihood. (f) Deconvolution by the Pixon method.

It is first worth pointing out that noise complicates the deconvolution problem: In its absence, simple Fourier methods suffice to directly invert (7) and recover the magnetization density $m(\boldsymbol{r'})$ in many cases. For nonzero noise, direct inversion is still possible provided one takes care to filter out noise-derived Fourier components that appear at high spatial frequency. Fig. 8(d) shows the result of such a direct inversion, accomplished through application of the well-known Wiener optimal filter technique to the data of Fig. 8(c). One immediately sees the effect of measurement noise on the reconstruction by comparison of Fig. 8(d) with the truth image of Fig. 8(b): Resolution is substantially lost and the reconstruction is plagued by noise-related artifacts. This level of performance is typical of such *linear* deconvolution techniques.

An alternative approach is to attempt to fit the data directly using a maximum-likelihood technique. Specifically, one seeks to minimize the chi-square fit statistic

$$\chi^2 = \sum_{i=1}^{N} \frac{\left[\left(\sum_{j=1}^{N} K_{i-j} I_j \right) - d_i \right]^2}{\sigma_i^2} \qquad (8)$$

with respect to the $N = 32^3$ voxel amplitudes I_j, where K_{i-j} is a discretized version of the MRFM point-response function, d_i is the measured datum at the $i$the probe position, and σ_i is the rms noise at that position (taken in our example to be a known constant independent of i). Fig. 8(e) shows the result of such a maximum-likelihood reconstruction. The computation is performed by setting initial values of the I_j to zero and undertaking a conjugate gradient minimization of (8) with the I_j as adjustable parameters. In the particular case of the result of Fig. 8(e), an additional constraint has been imposed that all image values must be nonnegative. One immediately sees a significant improvement in performance relative to the direct inversion Fourier techniques: Greater recovered resolution is obtained and much of the spurious noise has been eliminated. Figure 8(e) still exhibits spurious signals not present in the truth image, begging the question as to whether still better reconstruction procedures are available. The answer lies in the subject of nonlinear image reconstruction, a topic that is too large and complex to review here. Nevertheless, Fig. 8(f) shows the results obtained from one of the best nonlinear techniques in current use. Developed originally for applications in observational

astronomy and now in widespread use in that community, the Pixon method [19]–[21] of image reconstruction applies a "minimum complexity" principle to further constrain the set of all possible inversions of (7) when noise is present in the data. In essence, the Pixon method finds the smoothest, least structured, "least informative" image that is statistically consistent with the measured data. Like a maximum-likelihood technique, the Pixon method minimizes the chi-square fit statistic

$$\chi^2 = \sum_{i=1}^{N} \frac{\left[\left(\sum_{j=1}^{N} K_{i-j}\left[\sum_{k=1}^{N} \Pi_{jk}\phi_k\right]\right) - d_i\right]^2}{\sigma_i^2} \quad (9)$$

with respect to the $N = 32^3$ parameters ϕ_k, but subject to the constraints imposed by local smoothing kernels Π_{jk}. A different smoothing kernel—usually circular or spherical in footprint and parabolic in shape—resides on every grid point of the ϕ matrix. The diameter of the footprint varies from point to point depending upon the length scale of the local image structure: affiliated with large regions of constant intensity will be large-diameter kernels and *vice versa*. A minimum complexity solution results when a set of smoothing kernels with the largest possible diameters is found yet which still permit a good fit to the data. Implicit in this procedure is the need to objectively determine the kernel diameters prior to minimization. This can be accomplished in general by assuming some initial set of Π_{jk} with large footprints, minimizing (9) with respect to the ϕ_k, and then using the resulting image

$$I_j = \sum_{k=1}^{N} \Pi_{jk}\phi_k \quad (10)$$

to generate updated Π_{jk}. One then iterates until a good fit to the data is obtained. A faster, alternative approach is to simply use the results of a maximum-likelihood reconstruction to evaluate the Π_{jk} in a single step, insert these into (9), and then solve for ϕ_k. The final image is given again by (10). The result shown in Fig. 8(f) is obtained with this single-step procedure using the result of Fig. 8(e) as input to compute the diameters of the Pixon smoothing kernels. We find this method can yield improvements in linear resolution by factors of 2 to 3 and improvements in sensitivity to weak image sources by factors of 10 to 100 relative to competing techniques.

VIII. CONCLUSION

Magnetic-resonance force microscopy is an extremely promising technique that holds significant promise in applications for the study of spin injection devices, ferromagnetic systems, and semiconducting devices. However, several advances are necessary in order to make this technique useful to the general scientific community. In particular, a reliable technique for fabrication of micromagnets with known magnetic characteristics must be developed. This is essential for reliable 3-D subsurface image deconvolution. The micromagnet must, in turn, be integrated with the high-frequency micromechanical resonator that will allow wide-bandwidth data acquisition rates. We and others are presently pursuing these challenging tasks.

REFERENCES

[1] S. A. Wolf, D. D. Awschalom, R. A. Buhrman, J. M. Daughton, S. von Molnár, M. L. Roukes, A. Y. Chtchelkanova, and D. M. Treger, "Spintronics: A spin-based electronics vision for the future," *Science*, vol. 294, p. 1488, 2001.

[2] Y. Ohno, D. Young, B. Beschoten, F. Matsukura, H. Ohno, and D. Awschalom, "Electrical spin injection in a ferromagnetic semiconductor heterostructure," *Nature*, vol. 402, p. 790, 1999.

[3] R. Fiederling, M. Keim, G. Reuscher, W. Ossau, G. Schmidt, A. Waag, and L. Molenkamp, "Injection and detection of a spin-polarized current in a light-emitting diode," *Nature*, vol. 402, p. 787, 1999.

[4] J. A. Sidles, "Noninductive detection of single-proton magnetic resonance," *Appl. Phys. Lett.*, vol. 58, p. 2854, 1991.

[5] ——, "Folded Stern–Gerlach experiment as a means for detecting nuclear magnetic resonance in individual nuclei," *Phys. Rev. Lett.*, vol. 68, p. 1124, 1992.

[6] D. Rugar, C. S. Yannoni, and J. A. Sidles, "Mechanical detection of magnetic resonance," *Nature*, vol. 360, p. 563, 1992.

[7] P. C. Hammel, Z. Zhang, G. J. Moore, and M. L. Roukes, "Subsurface imaging with the magnetic resonance force microscope," *J. Low Temp. Phys.*, vol. 101, p. 59, 1995.

[8] D. Rugar, O. Züger, S. T. Hoen, C. S. Yannoni, H.-M. Vieth, and R. D. Kendrick, "Force detection of nuclear magnetic resonance," *Science*, vol. 264, p. 1560, 1994.

[9] Z. Zhang, P. C. Hammel, and P. E. Wigen, "Observation of ferromagnetic resonance using magnetic resonance force microscopy," *Appl. Phys. Lett.*, vol. 68, p. 2005, 1996.

[10] Z. Zhang, P. C. Hammel, M. Midzor, M. L. Roukes, and J. R. Childress, "Ferromagnetic resonance force microscopy on microscopic Co single layer films," *Appl. Phys. Lett.*, vol. 73, p. 2036, 1998.

[11] J. A. Sidles and D. Rugar, "Signal-to-noise ratios in inductive and mechanical detection of magnetic resonance," *Phys. Rev. Lett.*, vol. 70, p. 3506, 1993.

[12] Z. Zhang, M. L. Roukes, and P. C. Hammel, "Sensitivity and spatial resolution for electron-spin-resonance detection by magnetic resonance force microscopy," *J. Appl. Phys.*, vol. 80, p. 6931, 1996.

[13] A. Suter, D. V. Pelekhov, M. L. Roukes, and P. C. Hammel, "Probe-sample coupling in the magnetic resonance force microscope," *J. Magn. Reson.*, vol. 154, p. 210, 2002.

[14] M. M. Midzor, P. E. Wigen, D. V. Pelekhov, W. Chen, P. C. Hammel, and M. L. Roukes, "Imaging mechanism of force detected FMR microscopy," *J. Appl. Phys.*, vol. 87, p. 6493, 2000.

[15] M. Midzor, "Ferromagnetic resonance force microscopy," Ph.D. dissertation, Calif. Inst. Technol., Pasadena, CA, 2000.

[16] R. Damon and J. Eshbach, "Magnetostatic modes of a ferromagnetic slab," *J. Phys. Chem. Solids*, vol. 19, p. 308, 1961.

[17] B. E. Storey, A. O. Tooke, A. P. Cracknell, and J. A. Przystawa, "Determination of frequencies of magnetostatic modes in rectangular thin-films of ferrimagnetic Yttrium Iron-Garnet," *J. Phys. C—Solid State Physics*, vol. 10, p. 875, 1977.

[18] B. A. Kalinikos, "Excitation of propagating spin-waves in ferromagnetic films," *Proc. Inst. Elec. Eng.*, pt. H, vol. 127, p. 4, 1980.

[19] R. K. Piña and R. C. Puetter, "Bayesian image reconstruction: The Pixon method and optimal image modeling," *Publ. Astron. Soc. Pac.*, vol. 105, p. 630, 1993.

[20] R. C. Puetter, "Pixon-based multiresolution image reconstruction and the quantification of picture information content," *Int. J. Syst. Tech.*, vol. 6, p. 314, 1995.

[21] R. C. Puetter and A. Yahil, *Astronomical Data Analysis Software and Systems VIII*, D. M. Mehringer, R. L. Plante, and D. A. Roberts, Eds.   San Francisco, CA: Astron. Soc. Pacific, 1999, vol. 172, ASP Conf. Ser., p. 307.

P. Chris Hammel received the B.A. degree from the University of California, San Diego, La Jolla, and the Ph.D. degree from Cornell University, Ithaca, NY, with Robert Richardson, in 1984 for magentic resonance studies of magnetic coupling into the sub-millikelvin regime.

He is presently a Full Professor in the Physics Department at Ohio State University, Columbus, and an Ohio Eminent Scholar. His current research is focused on the development of ultra-high sensitivity magnetic-resonance force microscope with the goal of single-spin detection, and its application to solid-state quantum computing and imaging in magentic systems, including high-T_c cuprates and heavy fermions. He has presented over 70 invited talks including seven at the American Physical Society's March meeting, and five at Gordon conferences. He has over 75 publications in peer-reviewed journals that have been cited more than 1700 times and has authored two book chapters.

Denis V. Pelekhov, photograph and biography not available at the time of publication.

Philip E. Wigen (Member, IEEE) received the B.S. degree in chemistry from Pacific Lutheran University, Tacoma, WA, in 1955 and the Ph.D. degree in physics from Michigan State University, East Lansing, in 1960.

He was a Research Scientist with the Lockheed Research laboratories, Palo Alto, CA, from 1960 to 1995, where he initiated his work on ferromagnetic resonance in magnetic metal films. In 1965, he joined the Physics Faculty of the Ohio State University, Columbus, where he continued his work on the dynamical properties of ferromagnetic materials including ferromagnetic resonance, magnetic domainwall resonance, and chaos in magnetic systems. His recent work in magnetic-resonance force microscopy has be pursued in collaboration with the Roukes' group at the California Institute of Technology, Pasadena, where he holds a visiting professorship.

Prof. Wigen is a Fellow of the American Physical Society.

Timothy R. Gosnell is currently Chief Scientist at Pixon LLC, Setauket, NY, a private company that specializes in software and hardware products for high-performance image processing. This follows his long career as an experimental physicist working at Los Alamos National Laboratory, Los Alamos, NM, where he focused on problems in ultrafast laser physics and spectroscopy, optical physics and applications of rare-earth-doped insulators, and most recently, magnetic-resonance force microscopy. He has published over 50 articles and several books on these subjects.

Melissa M. Midzor received the Ph.D. degree in physics from the California Institute of Technology, Pasadena, in 2000.

Currently, she works for the U.S. Department of the Navy, Naval Air Warfare Center Weapons Division (NAVAIR)

Michael L. Roukes received the B.A. degree with a double major of physics and chemistry from the University of California, Santa Cruz, in 1978 and the M.S. and Ph.D. degrees in physics from Cornell University, Ithaca, NY, in 1985.

He was a Member of Technical Staff/Principal Investigator at Bell Communications Research, Livingstone, NJ. Since 1992, he has been Professor of physics, applied physics, and bioengineering at the California Institute of Technology (Caltech), Pasadena, where he has developed an extensive research program utilizing nanomechanical and nanoelectronic devices as interfaces into the worlds of single-spin dynamics and quantum information, biomolecular detection and imaging, ultrasensitive mass spectrometry, and ultrasensitive calorimetry. In 2002, he was selected from the "Frontiers of Engineering" programs as a Lillian Gilbreth Lecturer by the National Academy of Engineering.

Dr. Roukes is a Fellow of the American Physical Society and a Cofounder of Nanokinetics Corporation.